ACS APPLIED MATERIALS & INTERFACES

www.acsami.org

Research Article

Direct Tellurization of Pt to Synthesize 2D $PtTe_2$ for High-Performance Broadband Photodetectors and NIR Image Sensors

Xiao-Wei Tong, Ya-Nan Lin, Rui Huang, Zhi-Xiang Zhang, Can Fu, Di Wu, Lin-Bao Luo,* Zhong-Jun Li,* Feng-Xia Liang, and Wei Zhang*

Cite This: https://dx.doi.org/10.1021/acsami.0c14996

Read Online

ACCESS | Metrics & More | Article Recommendations | Supporting Information

ABSTRACT: Platinum telluride ($PtTe_2$) has garnered significant research enthusiasm owing to its unique characteristics. However, large-scale synthesis of $PtTe_2$ toward potential photoelectric and photovoltaic application has not been explored yet. Herein, we report direct tellurization of Pt nanofilms to synthesize large-area $PtTe_2$ films and the influence of growth conditions on the morphology of $PtTe_2$. Electrical analysis reveals that the as-grown $PtTe_2$ films exhibit typical semimetallic behavior, which is in agreement with the results of first-principles density functional theory (DFT) simulation. Moreover, the combination of multilayered $PtTe_2$ and Si results in the formation of a $PtTe_2$/Si heterojunction, exhibiting an obvious rectifying effect. Moreover, the $PtTe_2$-based photodetector displays a broadband photoresponse to incident radiation in the range of 200−1650 nm, with the maximum photoresponse at a wavelength of ∼980 nm. The R and D^* of the $PtTe_2$-based photodetector are found to be 0.406 A W^{-1} and 3.62×10^{12} Jones, respectively. In addition, the external quantum efficiency is as high as 32.1%. On the other hand, the response time of τ_{rise} and τ_{fall} is estimated to be 7.51 and 36.7 μs, respectively. Finally, an image sensor composed of a 8 × 8 $PtTe_2$-based photodetector array was fabricated, which can record five near-infrared (NIR) images under 980 nm with a satisfying resolution. The result demonstrates that the as-prepared $PtTe_2$ material will be useful for application in NIR optoelectronics.

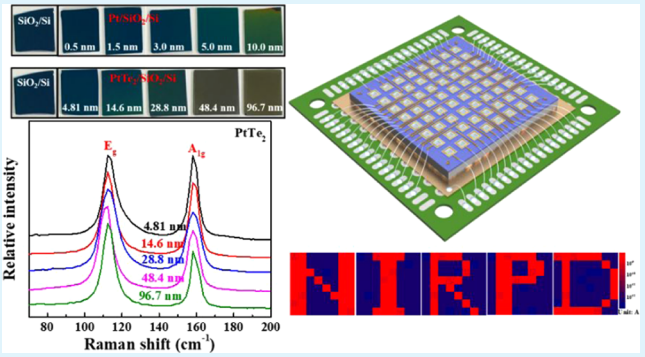

KEYWORDS: *NIR image sensors, platinum telluride, broadband photodetectors, heterojunctions, transition metal dichalcogenides*

INTRODUCTION

Transition metal dichalcogenides (TMDs) with a general stoichiometric formula of MR_2 (M = group 4−10 metals, R = O, S, Se, Te) are characterized by a layered structure with weak bonding forces between neighboring layers, and each layer has much strong bonding or ionic bonds between the metal and chalcogen atoms.[1,2] Since the first exfoliation of graphene in 2004,[3] two-dimensional (2D) TMDs have also inspired tremendous global research interest. To date, a huge number of 2D TMDs (e.g., WS_2,[4,5] WSe_2,[6] MoS_2,[7,8] $MoSe_2$,[9,10] $PtSe_2$,[11,12] $PdSe_2$,[13,14] etc.), have been successfully fabricated by either liquid assisted or mechanical exfoliation,[15] and these 2D TMDs have indeed exhibited various intriguing optical and optoelectronic properties,[16] such as tunable bandgap,[17,18] perfect surface,[19] prominent mechanical flexibility,[20] and outstanding carrier mobility.[21,22] Among the huge TMD family, $PtTe_2$ is a very special member due to its intriguing type-II Dirac fermions.[23,24] Thanks to this fantastic feature, $PtTe_2$ has proved to be one of the most important candidates for optoelectronics.[25,26] In addition, the absence of dangling bonds due to naturally terminated surfaces is beneficial for ambient stability, which might help protect the $PtTe_2$ device from surface-induced performance degradation.[27]

To date, ultrathin $PtTe_2$ layers in the form of nanosheets or nanofilm have been fabricated by various approaches, including chemical transformations,[28] chemical vapor deposition (CVD),[29] and mechanical or liquid assisted exfoliation.[30] For instance, Hao and colleagues, have developed a eutectic solidification technique to grow 2−200 nm thick, single-crystalline $PtTe_2$ nano-flakes. Moreover, they have demonstrated that the $PtTe_2$ sample exhibited an exceptionally high conductivity of 3.30×10^6 S m^{-1}.[31] Liu's group have reported a reliable epitaxy method to synthesize an ultrathin high-quality $PtTe_2$ film on mica. It was observed that the $PtTe_2$ device displayed a record electrical conductivity of 10^7 S m^{-1}, nearly one thousand times larger than that of 1T MoS_2.[32] Very recently,

Received: August 21, 2020
Accepted: November 5, 2020

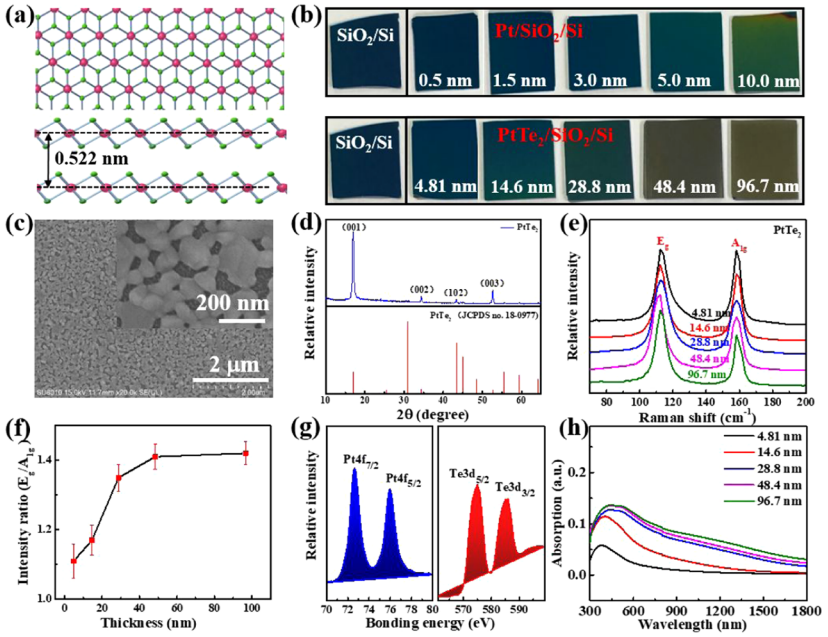

Figure 1. (a) Schematic of the $PtTe_2$ crystal structure with two different viewpoints (the top one is the vertical view and bottom one is the lateral view), Pt and Te atoms are labeled in red and green, respectively. (b) Digital photograph of Pt films with different thicknesses and corresponding $PtTe_2$ nanofilms onto SiO_2/Si. (c) FESEM image of the 28.8 nm $PtTe_2$ film, the inset shows a magnified FESEM image. (d) XRD analysis of the $PtTe_2$ sample. (e) Raman spectra of the $PtTe_2$ film with different thicknesses, a 532 nm excitation laser was used. (f) The relationship between the relative intensity ratio (E_g/A_{1g}) and the thickness of the $PtTe_2$ sample. (g) High-resolution Pt 4f and Te 3d XPS spectra of the as-synthesized $PtTe_2$ crystals. (h) Absorption spectra of $PtTe_2$ nanofilms with different thicknesses.

using a CVD method, Duan's group has successfully realized an efficient fabrication of $PtTe_2$ nanoplates, whose thickness can be tuned from 20.0 to 1.80 nm through scaling up carrier gas or reducing the reaction temperature. The as-synthesized sample showed an exceptionally high conductivity of 2.50×10^6 S m^{-1}.[33] In spite of tremendous progress made in material synthesis, there is no denying the fact that the majority of the $PtTe_2$ samples derived from these methods are composed of a huge number of small nanosheets or nanocrystals, with sizes usually less than 20 μm. This difficulty in accessing wafer-scale $PtTe_2$ films is the main obstacle for its further practical device application. Large-scale synthesis of highly crystalline $PtTe_2$ nanofilms, which are of paramount importance for new integrated optoelectronic device application, is thereby in great demand.

Herein, we present a facile, controllable, and large-scale preparation of a $PtTe_2$ thin film with thickness ranging from 4.81 to 96.7 nm by directly tellurizing a platinum film in a CVD system. During the synthesis, both tellurization temperature and carrier gas can influence the surface structure and chemical purity of $PtTe_2$. Directly combining the $PtTe_2$ film with Si will form a $PtTe_2$/Si heterojunction that exhibited an apparent rectifying effect. Further device analysis revealed that the $PtTe_2$/Si heterojunction photodetectors displayed a broadband photoresponse to light illumination ranging from 200 to 1650 nm, with peak photosensitivity at ~980 nm. The maximum responsivity (R), specific detectivity (D^*), and external quantum efficiency (EQE) of the $PtTe_2$/Si-device under 980 nm light irradiation, according to our further calculation, is determined to be 0.406 A W^{-1}, 3.62×10^{12} Jones, and 32.1%, respectively. Moreover, the response time (τ_r and τ_f) of the $PtTe_2$/Si-based near-infrared photodetector (NIRPD) can approach 7.51 and 36.7 μs, respectively. Finally, an image sensor which is composed of an 8 × 8 $PtTe_2$/Si heterojunction device array was fabricated. It is found that the image sensor can readily record five NIR images produced by 980 nm with content resolution.

RESULTS AND DISCUSSION

Figure 1a schematically illustrates the crystal structure of $PtTe_2$ with both top and lateral views. Basically, platinum telluride has a typical hexagonal structure: The waved Te−Pt−Te atomic layers are held by vdW interaction in a unique hexagonal way. The spacing between two adjacent layers is estimated to be about 0.522 nm.[31] Figure 1b displays a series of digital photographs of $PtTe_2$ films with layer thicknesses ranging from 4.81 to 96.7 nm, which are derived by directly tellurizing different thicknesses of platinum nanofilms (0.5−10.0 nm). It is obvious that after tellurization the color of the $PtTe_2$ film is found to evolve from navy to green-gray, as the thickness gradually increases from 4.81 to 96.7 nm. It should be noted that the thickness expansion factor, which is defined by the thickness of $PtTe_2$ over that of the Pt film precursor, is estimated to be 9.60, much larger than what was observed in $PtSe_2$ (2.90) and $PdSe_2$ (4.10).[34,35] Understandably, this relatively large value should be associated with the bigger atomic radius of Te over that of Se atoms. Moreover, field-emission SEM observation was carried out to study the thickness-dependent surface structure of as-tellurized $PtTe_2$ nanofilms. Figure 1c exhibits a typical FESEM image of the 28.8 nm $PtTe_2$ film, from which one can easily see that the thin film has a rough surface (the roughness of the $PtTe_2$ film with different thicknesses are shown in Figure S1). Furthermore, the FESEM image at higher magnification confirms that the thin film actually consists of innumerous nanoparticles, with diameters in the range of 40−200 nm (the inset of Figure 1c). Decreasing or increasing the thickness of the Pt precursor will lead to the formation of $PtTe_2$, however, in the form of either isolated nanoparticles or a thick network-like film

https://dx.doi.org/10.1021/acsami.0c14996
ACS Appl. Mater. Interfaces XXXX, XXX, XXX−XXX

(Figure S2). From the XRD analysis shown in Figure 1d, all signals are due to the hexagonal-phase $PtTe_2$ (JCPDS no. 18-0977, $a = b = 0.403$ nm, $c = 0.522$ nm).[31] As a matter of fact, the thickness of monolayer $PtTe_2$ can also be accurately extracted from the measurement of the electronic polarisability,[11] which is still in progress.

Furthermore, the Raman spectra in Figure 1e exhibits two obvious peaks corresponding to different vibrational modes of $PtTe_2$. The first strong peak at 112.4 cm^{-1} is due to the vibrational mode of in-plane Te−Pt−Te, while another peak at 158.1 cm^{-1} can be ascribed to the out-of-plane mode.[31] Interestingly, no obvious change in the Raman shift has been observed with increasing thickness of $PtTe_2$ from 4.81 to 48.4 nm. However, the relative intensity ratio (E_g/A_{1g}) increases from 1.12 to 1.41, and attains a saturation, irrespective of the further increase of thickness to 96.7 nm. This finding is probably due to the attenuated out-of-plane vibrational mode of thicker films. From the X-ray photoelectron spectroscopy (XPS) characterization, as shown in Figures 1g and S3, the peaks at 72.6, 75.98, 575.08, and 586.08 eV are attributed to the orbitals of Pt $4f_{7/2}$, Pt $4f_{5/2}$, Te $3d_{5/2}$, and Te $3d_{3/2}$, respectively. The Pt/Te stoichiometric ratio was estimated to be 1.01/2, which is close to the ideal composition of $PtTe_2$. Figure 1h plots the absorption curve of $PtTe_2$ films with different thicknesses. It can be readily observed that with the increasing thickness, the $PtTe_2$ film can harvest incident light with the wavelength ranging from 300 to 1800 nm. However, as $PtTe_2$ nanofilm is thicker than 28.8 nm, light absorption starts to saturate. The thickness-dependent absorption behavior is in agreement with the theoretical result obtained by DFT calculations (Figure S4). In light of the fact that the $PtTe_2$ film is a semimetal and there is a trade-off between the light absorption and electrical transport properties, $PtTe_2$ with a thickness of about 28.8 nm will be chosen to assemble the device in the following sections.

A representative TEM image (Figure 2a) reveals a 28.8 nm $PtTe_2$ film that is composed of network-like nanoparticles. Selected-area electron diffraction (SAED) further demonstrates the polycrystalline quality of the sample (Figure 2b). From the energy-dispersive X-ray spectroscopy (EDS) analysis, the chemical composition of the as-synthesized sample is close to the ideal formula of $PtTe_2$, as the stoichiometric ratio of Pt/Te is determined to be 33.6:66.4 (Figure 2c). As a matter of fact, the homogenous composition of the as-tellurized $PtTe_2$ has also been confirmed by both multiple-area EDS (Figure 2d) and elemental mapping results (Figure 2e,g). As shown in Figure 2h,i, the high-resolution TEM (HRTEM) image signifies the well-defined crystalline quality. The lattice fringe in the HRTEM image was calculated to be 0.289 nm, which is readily ascribed to the (101) planes of $PtTe_2$.

It is also found that the purity of $PtTe_2$ is influenced by experimental conditions such as tellurization temperature and the gas flow rate. For instance, pure $PtTe_2$ films can be easily obtained at tellurization temperatures of 773, 873, or 973 K. Nonetheless, obvious contaminants of Te appear once the tellurization temperature is increased to 1073 K, as shown in Figures S5 and S6. In addition to purity, the morphology of the product is highly affected by temperature as well. Figure S7 compares the FESEM images that are obtained by tellurizing a 3.0 nm Pt nanofilm at 773, 873, 973, and 1073 K, showing that only the sample derived at 873 K is composed of a continuous network-like $PtTe_2$, whereas samples tellurized at other temperature will be isolated crystals. On the other hand, the product can be influenced by the gas flow rate. As summarized in

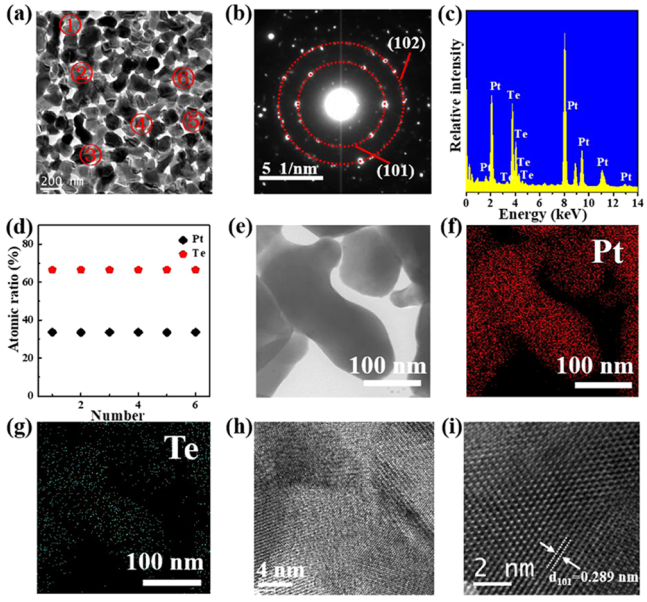

Figure 2. (a) A low-resolution TEM image of the $PtTe_2$ sample. (b) SAED image of the $PtTe_2$ sample. (c) EDX spectrum of the $PtTe_2$ sample. (d) Atomic ratio of six selected areas of the $PtTe_2$ sample. (e) TEM image of the $PtTe_2$ sample at high magnification. (f, g) Elemental mapping images of both platinum and tellurium elements. (h) HRTEM image of the $PtTe_2$ sample. (i) Magnified HRTEM image of the $PtTe_2$ sample.

Figure S8, when the 3.0 nm thick Pt nanofilm is tellurized at 773 K at different gas rates, e.g., 30.0, 50.0, 70.0, and 90.0 standard cubic centimeter per minute (SCCM), samples with different sizes of $PtTe_2$ nanoparticles are obtained. Overall, with the increase of the gas rate, the average diameter of $PtTe_2$ nanoparticles decreases. Meanwhile, the uniformity of $PtTe_2$ nanoparticles is improved. From the perspective of chemical dynamics, this finding is reasonable as slow transport of Te gas can lead to the formation of big nanoparticles at a low flow rate. On the contrary, fast transport of Te gas at a high flow rate may greatly facilitate mass growth of millions or even billions of small nanoparticles, thereby resulting in the formation of $PtTe_2$ nanoparticles with a relatively smaller diameter. Using Hall effect measurements, the conductivity of the $PtTe_2$ film (thickness of 28.8 nm) is estimated to be around 2.80×10^5 S m^{-1} at 300 K (thickness-dependent conductivity of the $PtTe_2$ nanofilms is provided in Figure S9), which is comparable to that of the $PtTe_2$ crystal derived by a CVD method (from 1.00×10^5 to 2.50×10^6 S m^{-1}) and single-crystal $PtTe_2$ nanosheets (10^7 S m^{-1}),[32,33] but much larger than that of PtS_2[36] and $PtSe_2$,[11] which can be ascribed to the semimetallic characteristics of $PtTe_2$.

To shed light on the electrical properties of the as-tellurized TMD materials, the electronic structures of $PtTe_2$ with different thicknesses were investigated. The schematic diagram in Figure 3a shows both top and side view of a 3×3 supercell of $PtTe_2$ with 3 layers. The blue dashed lines sketch the primitive cell. Figure 3b−e present the band structures of the $PtTe_2$ thin-films with 1-layer, 2-layer, 5-layer, and bulk, calculated at generalized-gradient approximation. It can be seen from the figures that the interlayer interactions exert substantial influence on the electronic structure of $PtTe_2$ thin films. For example, the $PtTe_2$ thin film obviously experiences a semiconducting-to-metallic transition when the film thickness increased to 2-layers. Such a metallic characteristic is consistent with the previously

https://dx.doi.org/10.1021/acsami.0c14996
ACS Appl. Mater. Interfaces XXXX, XXX, XXX−XXX

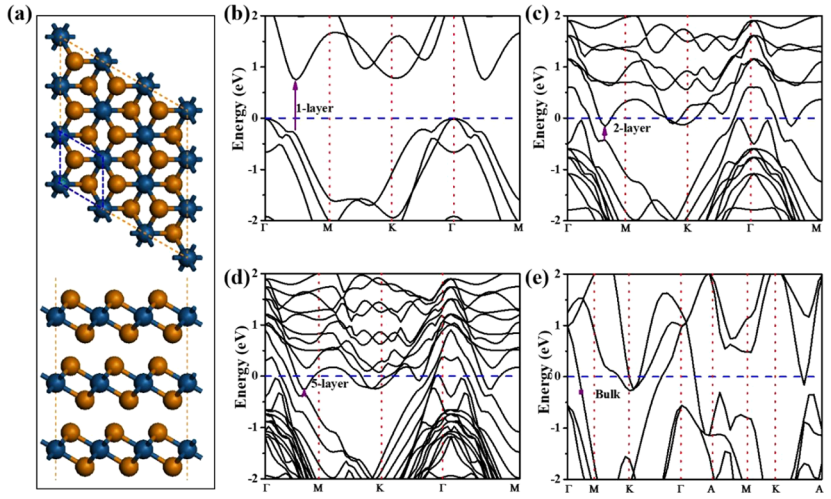

Figure 3. (a) Vertical and lateral view of a schematic exhibition of a 3-layer $PtTe_2$ supercell. The blue dashed lines sketch the primitive cell. Band structures of one-layer (b), two-layer (c), five-layer (d), and bulk (e) $PtTe_2$, purple arrows and square denote the gap evolution with thickness at a certain *k*-point.

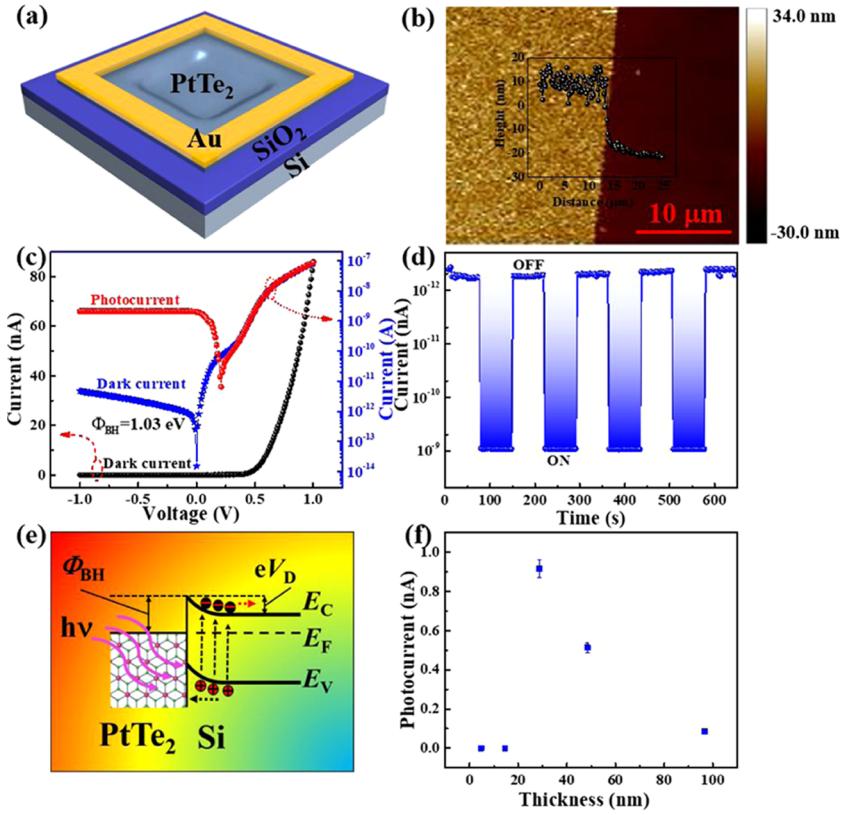

Figure 4. (a) Schematic of the $PtTe_2$/Si-based NIRPD. (b) AFM analysis of the $PtTe_2$/Si-device. (c) The current of the $PtTe_2$/Si-based NIRPD vs voltage with and without 980 nm illumination. (d) Photoresponse of the $PtTe_2$-based NIRPD under 980 nm illumination (94.6 $\mu W\ cm^{-2}$) at 0 V. (e) Energy band diagram of the $PtTe_2$/Si-device. (f) Photocurrent of the $PtTe_2$-based NIRPD based on different thicknesses of $PtTe_2$ nanofilm under 980 nm light illumination.

reported literature for $PtTe_2$.[23] One should note that the energy gap between two bands decreases with increasing thickness, as shown by purple arrows in Figure 3b–e. The decrease in the energy gap induces a red-shift of optical absorption peaks and strengthens the conductive characteristics of the thin film, which are in accordance with the abovementioned experimental measurement.

In addition, high-level theoretical methods, such as the HSE06 functional, are constantly employed to study the electronic structure of small systems. Spin–orbit coupling (SOC) may exert influence on the electronic structures for the present system with heavy atoms Pt and Te. Therefore, taking $PtTe_2$ bulk as an example, its band structures were comparatively calculated at the levels of PBE, PBE+SOC, and HSE06. As shown in Figure S10, the slight difference among them suggests that the GGA-PBE functional can predict a reliable trend of the electronic and optical properties of the $PtTe_2$ thin film.

https://dx.doi.org/10.1021/acsami.0c14996
ACS Appl. Mater. Interfaces XXXX, XXX, XXX−XXX

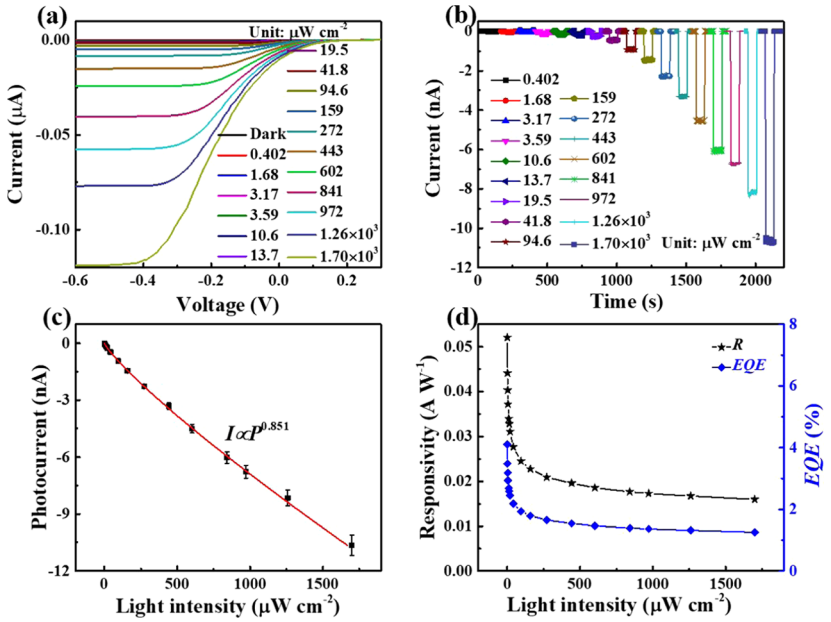

Figure 5. (a) The influence of light intensity on $I-V$ characteristics of NIRPD. (b) The influence of light intensity on $I-T$ characteristics of NIRPD. (c) The quantitative relationship between the photocurrent of the $PtTe_2$-based NIRPD and light intensity. (d) The evolution of R and EQE of the $PtTe_2$-based NIRPD corresponding to varying intensities.

The as-tellurized semimetal $PtTe_2$ film was then combined with Si to form a heterojunction photodetector, as illustrated in Figure 4a. The preparation procedure is provided in detail in the Experimental Section (Figure S11). From characterization using an atomic force microscope (AFM), the thickness of the $PtTe_2$ film obtained by directly tellurizing a 3.00 nm Pt nanofilm is ~28.8 nm (Figure 4b). The black curve shows the current−voltage characteristic of the $PtTe_2$/Si heterojunction without light illumination (Figure 4c), where the nonlinear behavior confirms a prominent rectifying behavior, where the rectification ratio can be estimated to be $\sim 10^4$ at ±1 V. The Schottky barrier of $PtTe_2$/Si is estimated to be 1.03 eV (detailed calculation is shown in the SI). This excellent rectification effect should be ascribed to the $PtTe_2$/Si heterojunction because of the negligible contact barrier of $PtTe_2$/Au and n-Si/In-Ga (Figure S12).[37] Once the $PtTe_2$/Si heterojunction was shined with 980 nm NIR light, it will display pronounced photovoltaic characteristics, in which the open-circuit voltage is ~0.210 V, and the short-circuit current is ~1.98 nA. However, despite the relatively low PCE, it can ensure the possibility for the $PtTe_2$/Si heterojunction to work at 0 V without external energy supply. Specifically, the photocurrent/dark current ratio (I_λ/I_d, λ refers to light wavelength) was estimated to be 2.01×10^3 (Figure 4d). As interpreted from the energy band diagram (Figure 4e), since the Fermi level of the $PtTe_2$ film is lower than that of Si, electrons in silicon will move to $PtTe_2$ when they are in contact, leading to the formation of a built-in electric field ($E_{built\text{-}in}$) at the $PtTe_2$/Si interface (depletion region). When the $PtTe_2$/Si device was shined with near-infrared light with an energy of >1.12 eV, photoexcited carriers will be separated in the depletion region, forming photocurrent in the device. As observed in other graphene-based optoelectronic devices,[38] the $PtTe_2$ film in this photodetector device mainly works as a semimetal electrode; on the one hand, it allows the transmittance of NIR light that will be absorbed by the underlying Si; on the other hand, it transports the holes after they were separated from the electric field. Owing to semimetallic behavior and the trade-off between light absorption and electrical conductivity mentioned above, only a 28.8 nm $PtTe_2$ film was chosen for device assembly, and it displayed the largest photocurrent compared to other thicknesses (Figure 4f).

To systematically explore the relationship between the photoelectric properties and NIR light, various intensity-dependent photoresponse measurement of the NIRPD under 980 nm irradiation was carried out. As displayed in Figure 5a,b, with the increase of light intensity from 0.402 to 1.70×10^3 μW cm^{-2}, the photocurrent gradually increased. Meanwhile, the dark current remained almost the same (Figure S13), resulting in an exceptionally high on/off ratio (>10^4). Then, a numerical power law, $I_\lambda = AP_\lambda^\theta$, was employed to numerically fit the dependent relationship between the NIR power and photocurrent, where θ is an exponent, A corresponds to a constant of 980 nm NIR light, and P_λ denotes the intensity of the 980 nm laser, respectively. By fitting the experimental results in Figure 5c, an exponent value of 0.851 for the $PtTe_2$-based NIRPD was obtained, indicating weak recombination activity due to the relatively low density of defect states.[39] Both R and EQE can be given as[40,41]

$$R = \frac{I_\lambda - I_d}{P_\lambda S} \quad (1)$$

$$\mathrm{EQE} = \frac{hcR}{e} \quad (2)$$

where e, S, I_λ, I_d, h, and c refer to the electronic charge, the effective NIR irradiation area, photocurrent, dark current, Planck's constant, and light-speed constant, respectively. Derived from both abovementioned formulas and experimental values ($I_\lambda = 8.93 \times 10^{-12}$ A, $I_d = 5.66 \times 10^{-13}$ A, $P_\lambda = 4.02 \times 10^{-7}$ W cm^{-2}, and $S = 4.00 \times 10^{-4}$ cm^2), R and EQE are respectively computed to be 0.0520 A/W and 4.11%. As shown in Figure 5d, by gradually increasing the intensity, both R and EQE were found to initially decrease and then reached a saturation level at a high light intensity. Such an evolution in the photocurrent is

https://dx.doi.org/10.1021/acsami.0c14996
ACS Appl. Mater. Interfaces XXXX, XXX, XXX−XXX

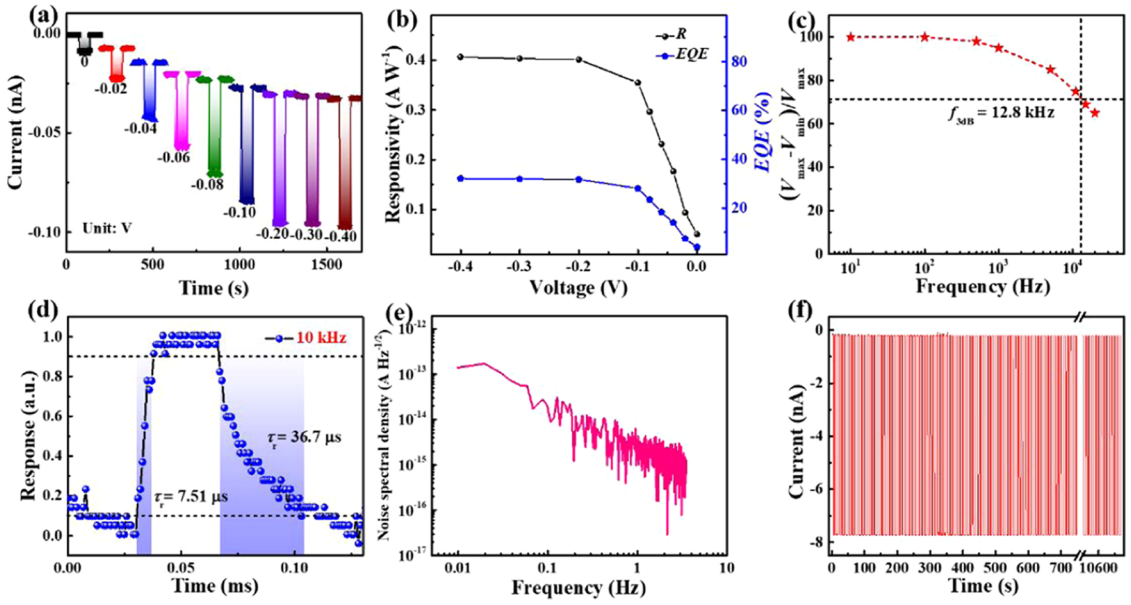

Figure 6. (a) Photoresponse of the $PtTe_2$-based NIRPD to 980 nm light (0.402 μW cm^{-2}) corresponding to varied bias voltages. (b) The influence of bias voltage on R and EQE of $PtTe_2$-based NIRPD. (c) $(V_{max} - V_{min})/V_{max}$ of NIRPD under a series of light frequencies. (d) Response cycle to estimate the rise and fall times. (e) The noise spectral density of the $PtTe_2$-based NIRPD analyzed by Fourier transform. (f) Photoresponse of the $PtTe_2$-based NIRPD for more than 1000 cycles.

Table 1. Comparison of the Figures of Merit of the Current $PtTe_2$-Based NIRPD with the Published Literature

device structure	R (A W^{-1})	D^* (Jones)	τ_r/τ_f (μs)	references
$PtSe_2$/Si	0.520	3.26×10^{13}	55.0/171	44
Bi_2Te_3/Si	0.017	2.50×10^{11}	$<1.00 \times 10^5$	48
Gr/CH_3−Si	0.328	6.03×10^{13}	22.0/56.0	47
Gr/Si	0.029	3.90×10^{11}	93.0/110	38
Gr/Si	0.400	5.40×10^{12}		45
$MoSe_2$/Si	0.270	7.13×10^{10}	0.270/0.350	50
MoS_2/Si	0.300	$\sim 1.00 \times 10^{13}$	3.00/40.0	46
Gr/Si	0.225	$\sim 1.00 \times 10^9$	$1.20 \times 10^3/3.00 \times 10^3$	49
$PtTe_2$/Si	0.406	3.62×10^{12}	7.51/36.7	this work

understandable because all of the photoexcited carriers can be effectively separated at low-light intensities. However, the concentration of photoinduced carriers increases sharply with increasing NIR intensity, and consequently, the recombination activity of carriers cannot be neglected accordingly. In particular, under a sufficient light intensity, the recombination activity of carriers started to undermine the photocurrent.[42]

Apart from the incident NIR intensity, the photoresponse of the $PtTe_2$-based NIRPD is also influenced by the bias voltage applied to the device. Figure 6a shows the photoresponse curve with t bias voltages ranging from −0.02 to −0.4 V, where the photocurrent dramatically increased with the decreasing voltage from zero bias to a reverse bias of −0.2 V, but remained unchanged when the voltage was further decreased to −0.4 V. Moreover, the dark current also exhibited the same tendency. The corresponding R and EQE with respect to bias voltages are shown in Figure 6b, from which both parameters are observed to increase initially and begin to saturate at 0.406 A/W and 32.1%, respectively, when the voltage is less than −0.2 V. Such a numerical evolution for both parameters is reasonable because the application of a reverse bias voltage on the $PtTe_2$/Si heterojunction strengthens the as-formed electric field by extending the depletion region. As a consequence, efficient separation of more photogenerated carriers takes place, leading to an increase in the photocurrent.[43,44] However, when all photogenerated carriers were completely separated, no more photogenerated can contribute to the photocurrent. As a result, the photocurrent begins to saturate, irrespective of the further increase in the bias voltage.

Our investigation also unveils that the present NIRPD is capable of detecting various swift-changing radiation signals with different frequencies, ranging from 500 Hz to 15 kHz (Figure S14). Figure 6c shows optical frequency-dependent relative balance $[(V_{max} - V_{min})/V_{max}]$. Apparently, the NIRPD can even monitor 10 kHz with excellent reproducibility. The 3 dB frequency $[(V_{max} - V_{min})/V_{max}$ reduces from the initial 1 to 0.707] is determined to be 12.8 kHz. Figure 6d presents a single enlarged cycle at 10 kHz, where τ_r (rise time)/τ_f (rise time) of 7.51/36.7 μs can be accurately determined. The specific detectivity (D^*) and noise equivalent power (NEP) are other two important parameters of photodetectors, which can be given as

$$D^* = \frac{(BS)^{1/2}}{\mathrm{NEP}} \tag{3}$$

$$\mathrm{NEP} = \frac{\overline{i_n^2}^{1/2}}{R} \tag{4}$$

https://dx.doi.org/10.1021/acsami.0c14996
ACS Appl. Mater. Interfaces XXXX, XXX, XXX−XXX

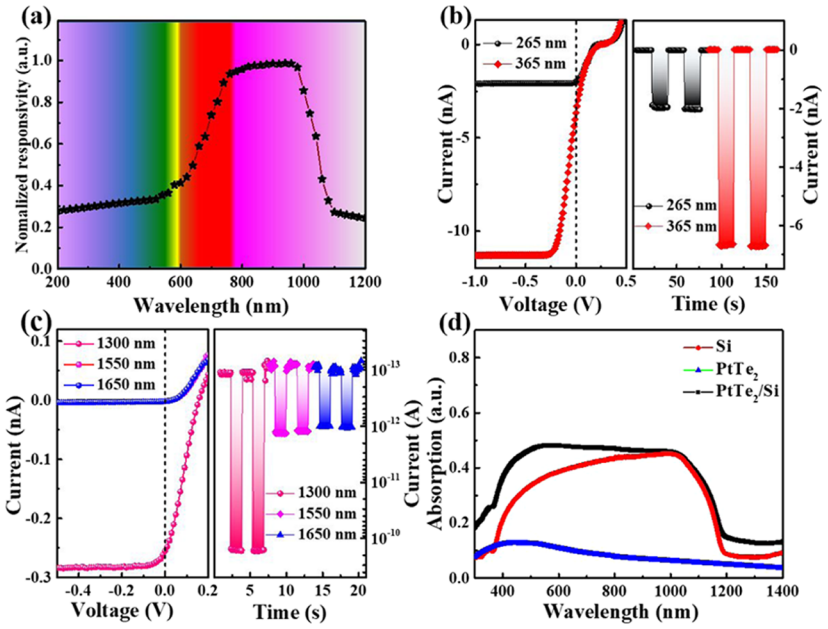

Figure 7. (a) Normalized responsivity of the $PtTe_2$/Si NIRPD at zero bias. (b) The photoresponse of the $PtTe_2$-device under 265 and 365 nm illumination. (c) The photoresponse curves of the $PtTe_2$-device under 1300, 1550, and 1650 nm light illumination. (d) The absorption spectra of silicon, $PtTe_2$ film, and $PtTe_2$/Si heterojunction.

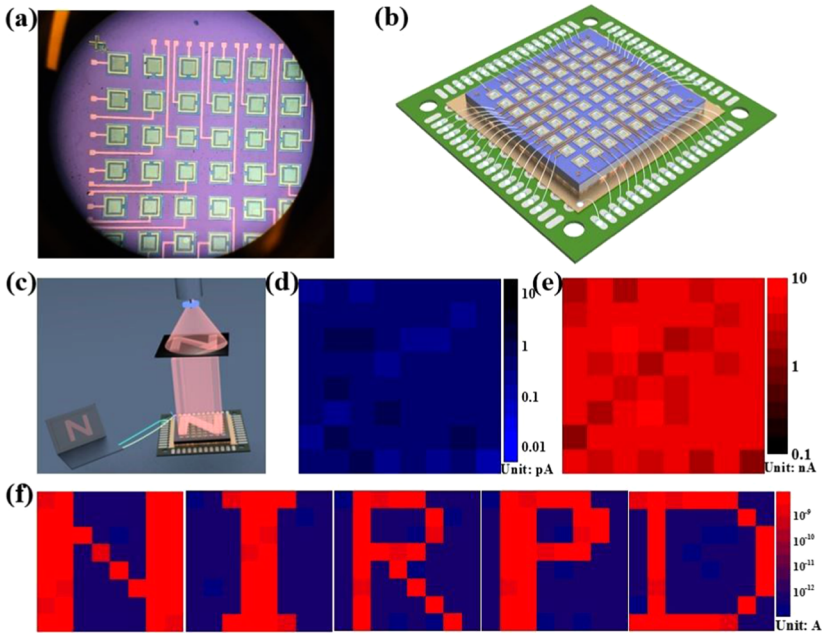

Figure 8. (a) Digital photograph and (b) schematic diagram of the $PtTe_2$-based NIRPD array. (c) Schematic illustration of the working mechanism of the $PtTe_2$-based image sensor. (d) The dark current of the $PtTe_2$-based NIRPD array. (e) Photocurrent of the NIRPD array under 980 nm light illumination. (f) The corresponding sensing results, where the image sensor was separately shined with five 980 nm illuminations with the shapes of "N", "I", "R", "P", and "D".

where B presents the bandwidth (1 Hz) and $\overline{i_n^2}^{1/2}$ denotes the root mean square value of the noise-current. The noise level per unit bandwidth (1 Hz) of the $PtTe_2$-based NIRPD, as displayed in Figure 6e, was determined to be $\sim 2.24 \times 10^{-15}$ A $Hz^{-1/2}$. Hence, the NEP and specific detectivity (D^*) are calculated to be 5.52×10^{-15} A W^{-1} $Hz^{-1/2}$ and 3.62×10^{12} Jones, respectively. Moreover, the $PtTe_2$/Si heterojunction can stably work under light illumination for more than 1000 cycles without obvious degradation (Figure 6f), suggesting good reproducibility.

Table 1 compares the key performance of the as-fabricated $PtTe_2$-based NIRPD and other previously reported silicon-based photodetectors. It can be easily found that while the responsivity was marginally lower than that of $PtSe_2$/Si,[44] and D^* was lower than those of $PtSe_2$/Si,[44] Gr/Si,[45] MoS_2/Si,[46] and Gr/CH_3-Si,[47] both parameters are much better than those of Bi_2Te_3/Si,[48] Gr/Si,[38,49] and $MoSe_2$/Si.[50] Moreover, the response time is faster than the majority of Si-based

https://dx.doi.org/10.1021/acsami.0c14996
ACS Appl. Mater. Interfaces XXXX, XXX, XXX−XXX

heterojunction device including $PtSe_2$/Si,[44] Bi_2Te_3/Si,[48] Gr/CH_3-Si,[47] and Gr/Si.[38,49] This optimal device performance suggests the potential application of the as-synthesized $PtTe_2$ materials in next-generation optoelectronic devices and systems.

Figure 7a displays the normalized photoresponse of the $PtTe_2$-based NIRPD to irradiation in the spectral range of 200−1200 nm. The as-prepared photodetector displays apparent photoresponse to the spectrum of 750−1000 nm but a relatively weak response to other irradiation with shorter and longer wavelengths, which is similar to the photoresponse of the Si-based photodetector. For instance, a relatively weak photovoltaic effect can still be found under 365 or 265 nm illumination, (Figure 7b). Although this effect is relatively weak, the NIRPD can still exhibit an apparent photoresponse with good reproducibility. Figure 7c shows the photoresponse of NIRPD under 1300, 1550, and 1650 nm illumination (~1 mW cm^{-2}). Specifically, the dark current is about 10^{-13} A, and the photocurrent under 1300 nm light illumination is around 1.40×10^{-10} A, leading to a high on/off ratio of 10^3. This value is much higher than that under both 1550 and 1650 nm illumination. Such broad photosensitivity is probably due to the contribution from $PtTe_2$ that exhibits typical long-range photon absorption capability, as revealed in Figure 7d.

The $PtTe_2$-based NIRPD array with 64 pixels was assembled on a SiO_2/Si wafer by lithography to explore the possibility of using the as-fabricated NIRPD for image sensing application. Figure 8a shows a typical microscopy image of the 8×8 $PtTe_2$/Si heterojunction device array (the typical size of each device is around 200×200 μm^2, the fabrication details are given in the Experimental Section), which was mounted onto a printed circuit board using a wire bonder (Figure 8b), contributing to further convenient characterization. The image sensing setup is schematically illustrated in Figure 8c. Five masks with different letters "N", "I", "R", "P", and "D" were separately placed between the NIR-LED (light-emitting diode) and the $PtTe_2$-based NIRPD array. During image sensing measurements, once the 980 nm LED was switched on, the light passed through the mask to directly project each word on the $PtTe_2$-based NIRPD array with 64 pixels. Figures 8d,e shows the current distribution of the 64 $PtTe_2$-based NIRPD without and with light illumination, respectively. The majority of the devices (>80%) exhibit a satisfying uniformity in photoelectric sensitivity. The five pictures in Figure 8f show the image sensing results, which were separately obtained by different characters mentioned above. It is clear that the shape of all of the five letters including "N", "I", "R", "P", and "D" can be easily seen due to their distinct contrast with the background, suggesting the tremendous potential of present $PtTe_2$-based NIRPD array in next-generation optoelectronics.

Our further device characterization unveils that the present $PtTe_2$/Si NIRPD exhibited superior device stability. Figure S15a compares the photosensing properties of the present heterojunction NIRPD, which was stored under ambient conditions for 2 months. We have not observed obvious degradation in the photocurrent, which can be ascribed to the superior stability of $PtTe_2$ in air, as revealed by both XRD pattern and Raman spectra in Figure S15b,c. As a matter of fact, this excellent device stability, according to a previous study is associated with the absence of dangling bonds owing to naturally terminated surfaces.[27]

CONCLUSIONS

We developed a facile tellurization approach for controlled synthesis of platinum telluride ($PtTe_2$) with different thicknesses, ranging from 4.81 to 96.7 nm. It has been demonstrated that the morphology and chemical composition are significantly influenced by the tellurization temperature and the gas flow rate. Moreover, the direct combination of $PtTe_2$ film and Si wafer leads to the formation of a $PtTe_2$/Si heterojunction, which displays a large rectification ratio of $\sim 10^4$. It is also revealed that the present $PtTe_2$/Si NIRPD exhibits broadband sensitivity in the wavelength of 200−1650 nm, with the peak photoresponse at around 980 nm. At this specific wavelength, the peak responsivity, specific detectivity, and external quantum efficiency were respectively calculated to be 0.406 A/W, 3.62×10^{12} Jones, and 32.1%. In addition, an image sensor which is composed of a 64 $PtTe_2$/Si heterojunction device array was fabricated. It is found that the image sensor can readily record five NIR images produced at 980 nm. The result suggests that the current $PtTe_2$ is a promising building block for the fabrication of future optoelectronics.

EXPERIMENTAL SECTION

Materials Preparation and Device Assembly. Platinum telluride in this study was synthesized by directly tellurizing a Pt nanofilm. In brief, lightly doped silicon (1−10 Ω cm), with a thin insulator layer (300 nm SiO_2) was rinsed with piranha solution [$V(H_2SO_4)/V(H_2O_2)$: 7/3], followed by ultrasonication in ultra-pure water, acetone, alcohol, and distilled water, separately. With the assistance of the photolithography process, the central part insulator layer of the as-cleaned Si/SiO_2 wafer was removed by a buffer oxidation solution (BOE, comprised of hydrofluoric acid, ammonium fluoride, and deionized water). Afterward, platinum films with different thicknesses ranging from 0.5 to 10.0 nm were deposited on exposed silicon by electron beam evaporation. The substrates loaded with the platinum film were then placed in the central part of a tube furnace, where a vessel with 0.100 g of tellurium powder was placed upstream. During the tellurization process, the oven was heated to 873 K and held for 1 h, then naturally cooled to 300 K. It should be noted that the tellurization process was carried out under an argon atmosphere with a flow rate of 90.0 SCCM. Finally, a 50.0 nm Au film was deposited on platinum telluride to form a circle electrode assisted with the third lithography.

Materials Characterization and Device Analysis. The absorption of the $PtTe_2$ sample was characterized by an ultraviolet−visible−near-infrared spectrophotometer (Cary 5000). The morphology and lattice structure of the $PtTe_2$ sample were observed by FESEM (SU8010) and HRTEM (JEM-2100F), and the acceleration voltage of the HRTEM was 200 kV. The thickness and roughness of the $PtTe_2$ sample were tested using an AFM (Dimension Icon). The layer structure and phase of the $PtTe_2$ sample were determined by a Raman spectrometer (LabRam HR Evolution, the power of the 530 nm laser is 0.400 mW) and an X-ray diffractometer (D/MAX2500VL/PC). The atomic ratio and composition of the $PtTe_2$ sample were studied by XPS analysis (Thermo, ESCALAB250Xi). The photoelectrical performances of the $PtTe_2$/Si-based NIRPD were analyzed by a Keithley-4200 and an oscilloscope (TDS2012B).

Computational Methods. All calculations were carried out using the Vienna ab initio simulation package (VASP) code[51] based on DFT.[52] The Perdew−Burke−Ernzerhof (PBE) functional of generalized-gradient approximation (GGA) was employed.[53] A cutoff energy of 500 eV was set for the plane-wave basis set. In the optimization of geometrical structure and calculation of the electronic structure, *k*-point sets of $11 \times 11 \times 1$ and $15 \times 15 \times 1$ were used for $PtTe_2$ thin films, and $8 \times 8 \times 6$ and $12 \times 12 \times 9$ were used for bulk $PtTe_2$, respectively. The convergence criteria for energy and force were set to be 10^{-5} eV and 0.01 eV/Å. A vacuum region of 20 Å normal to the surface of thin films was added to avoid the interaction between two adjacent periodic

https://dx.doi.org/10.1021/acsami.0c14996
ACS Appl. Mater. Interfaces XXXX, XXX, XXX−XXX

images. The vdW interaction was described by the DFT-D3 method of Grimme.[54]

■ ASSOCIATED CONTENT

Supporting Information

The Supporting Information is available free of charge at https://pubs.acs.org/doi/10.1021/acsami.0c14996.

AFM analysis of the $PtTe_2$ film tellurized at 873 K with different thicknesses; roughness of the $PtTe_2$ nanofilm with different thicknesses; FESEM images of the $PtTe_2$ sample with different thicknesses of 4.81, 14.6, 28.8, 48.4, and 96.7 nm tellurized at 773 K; XPS analysis of the as-synthesized $PtTe_2$ crystals; absorption coefficients of bulk, 5-layer, 2-layer, and 1-layer of $PtTe_2$; X-ray diffraction pattern of the $PtTe_2$ tellurized at different temperatures; Raman spectra of the $PtTe_2$ film tellurized at different temperatures; FESEM image of the $PtTe_2$ film tellurized at different temperatures; FESEM image of the $PtTe_2$ film tellurized at 873 K from the Pt film with a thickness of 3.0 nm under an argon gas atmosphere with flow rates of 30.0, 50.0, 70.0, and 90.0 SCCM; numerical distribution of $PtTe_2$ nanoparticle diameter in selected areas; conductivity as a function of thickness; energy band diagram of bulk $PtTe_2$ simulated at PBE, PBE+SOC, and HSE06 methods; schematic diagram of the fabrication procedure of $PtTe_2$/Si-based NIRPD; $I-V$ characteristics of the Au/$PtTe_2$/Au device without illumination; dark current of the $PtTe_2$/Si heterojunction under a series of intensities; the response of $PtTe_2$/Si NIRPD to fast-switching 980 nm light; photoresponse of $PtTe_2$/Si-based NIRPD was characterized at a time interval of 2 months; XRD characterization of the $PtTe_2$ sample after 2 months; and Raman spectra of the $PtTe_2$ film after storage in atmosphere for 2 months (PDF)

■ AUTHOR INFORMATION

Corresponding Authors

Lin-Bao Luo − *School of Electronic Science and Applied Physics, Hefei University of Technology, Hefei 230009, China;* orcid.org/0000-0001-8651-8764; Email: luolb@hfut.edu.cn

Zhong-Jun Li − *School of Electronic Science and Applied Physics, Hefei University of Technology, Hefei 230009, China*; Email: zjli@hfut.edu.cn

Wei Zhang − *Academy of Optoelectronic Technology, National Engineering Laboratory of Special Display Technology, Hefei University of Technology, Hefei 230009, China*; Email: zhangw@hfut.edu.cn

Authors

Xiao-Wei Tong − *School of Electronic Science and Applied Physics, Hefei University of Technology, Hefei 230009, China*

Ya-Nan Lin − *School of Electronic Science and Applied Physics, Hefei University of Technology, Hefei 230009, China*

Rui Huang − *School of Electronic Science and Applied Physics, Hefei University of Technology, Hefei 230009, China*

Zhi-Xiang Zhang − *School of Electronic Science and Applied Physics, Hefei University of Technology, Hefei 230009, China*

Can Fu − *School of Electronic Science and Applied Physics, Hefei University of Technology, Hefei 230009, China*

Di Wu − *School of Physics and Microelectronics, Zhengzhou University, Zhengzhou 450052, China;* orcid.org/0000-0003-3266-0612

Feng-Xia Liang − *School of Materials Science and Engineering, Anhui Provincial Key Laboratory of Advanced Functional Materials and Devices, Hefei University of Technology, Anhui 230009, China*

Complete contact information is available at: https://pubs.acs.org/10.1021/acsami.0c14996

Author Contributions

X.-W.T. designed and carried out the experiments, investigated the properties of the device, and completed the paper-writing. L.-B.L. and F.-X.L. supported the whole research process, analyzed the performance and internal mechanism, and revised the paper. Z.-J.L. carried out the theoretical calculation of $PtTe_2$, contributed to the writing of the theory section of the manuscript. Y.-N.L., R.H., Z.-X.Z., C.F., D.W., and W.Z. provided advice for improvement and jointed the discussion. All authors presented both advice and comment on the manuscript.

Notes

The authors declare no competing financial interest.

■ ACKNOWLEDGMENTS

This work was supported by the National Natural Science Foundation of China (NSFC, No. 62074048), the Fundamental Research Funds for the Central Universities (PA2020GDKC0014, JZ2020HGTB0051, and JZ2018HGXC0001), and the Open Foundation of Anhui Provincial Key Laboratory of Advanced Functional Materials and Devices (4500-411104/011).

■ REFERENCES

(1) Novoselov, K. S.; Mishchenko, A.; Carvalho, A.; Castro Neto, A. H. 2D Materials and van der Waals Heterostructures. *Science* **2016**, *353*, No. aac9429.

(2) Huang, X.; Zeng, Z. Y.; Zhang, H. Metal Dichalcogenide Nanosheets: Preparation, Properties and Applications. *Chem. Soc. Rev.* **2013**, *42*, 1934−1946.

(3) Novoselov, K. S.; Geim, A. K.; Morozov, S. V.; Jiang, D.; Zhang, Y.; Dubonos, S. V.; Grigorieva, I. V.; Firsov, A. A. Electric Field Effect in Atomically Thin Carbon Films. *Science* **2004**, *306*, 666−669.

(4) Duan, X.; Wang, C.; Shaw, J. C.; Cheng, R.; Chen, Y.; Li, H.; Wu, X.; Tang, Y.; Zhang, Q.; Pan, A.; Jiang, J.; Yu, R.; Huang, Y.; Duan, X. Lateral Epitaxial Growth of Two-Dimensional Layered Semiconductor Heterojunctions. *Nat. Nanotechnol.* **2014**, *9*, 1024−1030.

(5) Yang, Y.; Fei, H.; Ruan, G.; Li, Y.; Tour, J. M. Vertically Aligned WS_2 Nanosheets for Water Splitting. *Adv. Funct. Mater.* **2015**, *25*, 6199−6204.

(6) Zhou, H.; Wang, C.; Shaw, J. C.; Cheng, R.; Chen, Y.; Huang, X.; Liu, Y.; Weiss, N. O.; Lin, Z.; Huang, Y.; Duan, X. Large Area Growth and Electrical Properties of p-Type WSe_2 Atomic Layers. *Nano Lett.* **2015**, *15*, 709−713.

(7) Yu, Y.; Huang, S. Y.; Li, Y.; Steinmann, S. N.; Yang, W.; Cao, L. Layer-Dependent Electrocatalysis of MoS_2 for Hydrogen Evolution. *Nano Lett.* **2014**, *14*, 553−558.

(8) Zhang, X.; Lai, Z.; Tan, C.; Zhang, H. Solution-Processed Two-Dimensional MoS_2 Nanosheets: Preparation, Hybridization, and Applications. *Angew. Chem., Int. Ed.* **2016**, *55*, 8816−8838.

(9) Kong, D.; Wang, H.; Cha, J. J.; Pasta, M.; Koski, K. J.; Yao, J.; Cui, Y. Synthesis of MoS_2 and $MoSe_2$ Films with Vertically Aligned Layers. *Nano Lett.* **2013**, *13*, 1341−1347.

(10) Liang, J.; Zhang, J.; Li, Z.; Hong, H.; Wang, J.; Zhang, Z.; Zhou, X.; Qiao, R.; Xu, J.; Gao, P.; Liu, Z.; Liu, Z.; Sun, Z.; Meng, S.; Liu, K.; Yu, D. Monitoring Local Strain Vector in Atomic-Layered $MoSe_2$ by Second-Harmonic Generation. *Nano Lett.* **2017**, *17*, 7539−7543.

https://dx.doi.org/10.1021/acsami.0c14996
ACS Appl. Mater. Interfaces XXXX, XXX, XXX−XXX

(11) Tian, T.; Scullion, D.; Hughes, D.; Li, L. H.; Shih, C.-J.; Coleman, J.; Chhowalla, M.; Santos, E. J. G. Electronic Polarizability as the Fundamental Variable in the Dielectric Properties of Two-Dimensional Materials. *Nano Lett.* **2020**, *20*, 841−851.
(12) Wang, Y. L.; Li, L. F.; Yao, W.; Song, S. R.; Sun, J. T.; Pan, J. B.; Ren, X.; Li, C.; Okunishi, E.; Wang, Y. Q.; Wang, E. Y.; Shao, Y.; Zhang, Y. Y.; Yang, H. T.; Schwier, E. F.; Iwasawa, H.; Shimada, K.; Taniguchi, M.; Cheng, Z. H.; Zhou, S. Y.; Du, S. X.; Pennycook, S. J.; Pantelides, S. T.; Gao, H. J. Monolayer $PtSe_2$, A New Semiconducting Transition-Metal-Dichalcogenide, Epitaxially Grown by Direct Selenization of Pt. *Nano Lett.* **2015**, *15*, 4013−4018.
(13) Chow, W. L.; Yu, P.; Liu, F. C.; Hong, J. H.; Wang, X. L.; Zeng, Q. S.; Hsu, C. H.; Zhu, C.; Zhou, J. D.; Wang, X. W.; Xia, J.; Yan, J. X.; Chen, Y.; Wu, D.; Yu, T.; Shen, Z. X.; Lin, H.; Jin, C. H.; Tay, B. K.; Liu, Z. High Mobility 2D Palladium Diselenide Field-Effect Transistors with Tunable Ambipolar Characteristics. *Adv. Mater.* **2017**, *29*, No. 1602969.
(14) Oyedele, A. D.; Yang, S. Z.; Liang, L. B.; Puretzky, A. A.; Wang, K.; Zhang, J. J.; Yu, P.; Pudasaini, P. R.; Ghosh, A. W.; Liu, Z.; Rouleau, C. M.; Sumpter, B. G.; Chisholm, M. F.; Zhou, W.; Rack, P. D.; Geohegan, D. B.; Xiao, K. $PdSe_2$: Pentagonal Two-Dimensional Layers with High Air Stability for Electronics. *J. Am. Chem. Soc.* **2017**, *139*, 14090−14097.
(15) Butler, S. Z.; Hollen, S. M.; Cao, L. Y.; Cui, Y.; Gupta, J. A.; Gutie′rrez, H. R.; Heinz, T. F.; Hong, S. S.; Huang, J. X.; Ismach, A. F.; Johnston-Halperin, E.; Kuno, M.; Plashnitsa, V. V.; Robinson, R. D.; Ruoff, R. S.; Salahuddin, S.; Shan, J.; Shi, L.; Spencer, M. G.; Terrones, M.; Windl, W.; Goldberger, J. E. Progress, Challenges, and Opportunities in Two-Dimensional Materials Beyond Graphene. *ACS Nano* **2013**, *7*, 2898−2926.
(16) Mak, K. F.; Shan, J. Photonics and Optoelectronics of 2D Semiconductor Transition Metal Dichalcogenides. *Nat. Photonics* **2016**, *10*, 216−226.
(17) Long, M. S.; Wang, P.; Fang, H. H.; Hu, W. D. Progress, Challenges, and Opportunities for 2D Material Based Photodetectors. *Adv. Funct. Mater.* **2019**, *29*, No. 1803807.
(18) Susarla, S.; Kutana, A.; Hachtel, J. A.; Kochat, V.; Apte, A.; Vajtai, R.; Idrobo, J. C.; Yakobson, B. I.; Tiwary, C. S.; Ajayan, P. M. Quaternary 2D Transition Metal Dichalcogenides (TMDs) with Tunable Bandgap. *Adv. Mater.* **2017**, *29*, No. 1702457.
(19) Zhao, H. T.; Mu, X. L.; Zheng, C. H.; Liu, S. J.; Zhu, Y. Q.; Gao, X.; Wu, T. Structural Defects in 2D MoS_2 Nanosheets and Their Roles in the Adsorption of Airborne Elemental Mercury. *J. Hazard. Mater.* **2019**, *366*, 240−249.
(20) Gupta, A.; Sakthivel, T.; Seal, S. Recent Development in 2D Materials beyond Graphene. *Prog. Mater. Sci.* **2015**, *73*, 44−126.
(21) Lee, K. C.; Yang, S. H.; Sung, Y. S.; Chang, Y. M.; Lin, C. Y.; Yang, F. S.; Li, M. J.; Watanabe, K. J.; Taniguchi, T.; Ho, C. H.; Lien, C. H.; Lin, Y. F. Analog Circuit Applications Based on All-2D Ambipolar $ReSe_2$ Field-Effect Transistors. *Adv. Funct. Mater.* **2019**, *29*, No. 1809011.
(22) Ji, H. G.; Solís-Fernández, P.; Yoshimura, D.; Maruyama, M.; Endo, T.; Miyata, Y.; Okada, S.; Ago, H. Chemically Tuned p- and n-Type WSe_2 Monolayers with High Carrier Mobility for Advanced Electronics. *Adv. Mater.* **2019**, *31*, No. 1903613.
(23) Yan, M. Z.; Huang, H. Q.; Zhang, K. N.; Wang, E. Y.; Yao, W.; Deng, K.; Wan, G. L.; Zhang, H. Y.; Arita, M.; Yang, H. T.; Sun, Z.; Yang, H.; Wu, Y.; Fan, S. S.; Duan, W. H.; Zhou, S. Y. Lorentz-Violating Type-II Dirac Fermions in Transition Metal Dichalcogenide $PtTe_2$. *Nat. Commun.* **2017**, *8*, No. 257.
(24) Politano, A.; Chiarello, G.; Kuo, C. N.; Lue, C. S.; Edla, R. J.; Torelli, P.; Pellegrini, V.; Boukhvalov, D. W. Tailoring the Surface Chemical Reactivity of Transition-Metal Dichalcogenide $PtTe_2$ Crystals. *Adv. Funct. Mater.* **2018**, *28*, No. 1706504.
(25) Fu, D. Z.; Bo, X. Y.; Fei, F. C.; Wu, B.; Gao, M.; Wang, X. F.; Naveed, M.; Shah, S. A.; Bu, H. J.; Wang, B. G.; Cao, L.; Zou, W. Q.; Wan, X. G.; Song, F. Q. Quantum Oscillations in Type-II Dirac Semimetal $PtTe_2$. *Phys. Rev. B* **2018**, *97*, No. 245109.
(26) Zheng, W.; Schönemann, R.; Aryal, N.; Zhou, Q.; Rhodes, D.; Chiu, Y. C.; Chen, K. W.; Kampert, E.; Förster, T.; Martin, T. J.; McCandless, G. T.; Chan, J. Y.; Manousakis, E.; Balicas, L. Detailed Study of the Fermi Surfaces of the Type-II Dirac Semimetallic Candidates XTe_2 (X=Pd, Pt). *Phys. Rev. B* **2018**, *97*, No. 235154.
(27) Liang, Q. J.; Wang, Q. X.; Zhang, Q.; Wei, J. X.; Lim, S. X.; Zhu, R.; Hu, J. X.; Wei, W.; Lee, C. K.; Sow, C. H.; Zhang, W. J.; Wee, A. T. S. High-Performance, Room Temperature, Ultra-Broadband Photodetectors Based on Air-Stable $PdSe_2$. *Adv. Mater.* **2019**, *31*, No. 1807609.
(28) Moon, G. D.; Ko, S.; Xia, Y. N.; Jeong, U. Chemical Transformations in Ultrathin Chalcogenide Nanowires. *ACS Nano* **2010**, *4*, 2307−2319.
(29) Zhang, Y.; Yao, Y. Y.; Sendeku, M. G.; Yin, L.; Zhan, X. Y.; Wang, F.; Wang, Z. X.; He, J. Recent Progress in CVD Growth of 2D Transition Metal Dichalcogenides and Related Heterostructures. *Adv. Mater.* **2019**, *31*, No. 1901694.
(30) Tan, C. L.; Zhang, H. Two-Dimensional Transition Metal Dichalcogenide Nanosheet-based Composites. *Chem. Soc. Rev.* **2015**, *44*, 2713−2731.
(31) Hao, S.; Zeng, J. W.; Xu, T.; Cong, X.; Wang, C. Y.; Wu, C. C.; Wang, Y. J.; Liu, X. W.; Cao, T. J.; Su, G. X.; Jia, L. X.; Wu, Z. T.; Lin, Q.; Zhang, L. L.; Yan, S. N.; Guo, M. F.; Wang, Z. L.; Tan, P. H.; Sun, L. T.; Ni, Z. H.; Liang, S. J.; Cui, X. Y.; Miao, F. Low-Temperature Eutectic Synthesis of $PtTe_2$ with Weak Antilocalization and Controlled Layer Thinning. *Adv. Funct. Mater.* **2018**, *28*, No. 1803746.
(32) Fu, L.; Hu, D. B.; Mendes, R. G.; Rummeli, M. H.; Dai, Q.; Wu, B.; Fu, L.; Liu, Y. Q. Highly Organized Epitaxy of Dirac Semimetallic $PtTe_2$ Crystals with Extrahigh Conductivity and Visible Surface Plasmons at Edges. *ACS Nano* **2018**, *12*, 9405−9411.
(33) Ma, H. F.; Chen, P.; Li, B.; Li, J.; Ai, R. Q.; Zhang, Z. W.; Sun, G. Z.; Yao, K. K.; Lin, Z. Y.; Zhao, B.; Wu, R. X.; Tang, X. W.; Duan, X. D.; Duan, X. F. Thickness-Tunable Synthesis of Ultrathin Type-II Dirac Semimetal $PtTe_2$ Single Crystals and Their Thickness-Dependent Electronic Properties. *Nano Lett.* **2018**, *18*, 3523−3529.
(34) Zeng, L. H.; Lin, S. H.; Li, Z. J.; Zhang, Z. X.; Zhang, T. F.; Xie, C.; Mak, C. H.; Chai, Y.; Lau, S. P.; Luo, L. B.; Tsang, Y. H. Fast, Self-Driven, Air-Stable, and Broadband Photodetector Based on Vertically Aligned $PtSe_2$/GaAs Heterojunction. *Adv. Funct. Mater.* **2018**, No. 1705970.
(35) Luo, L. B.; Wang, D.; Xie, C.; Hu, J. G.; Zhao, Z. Y.; Liang, F. X. $PdSe_2$ Multilayer on Germanium Nanocones Array with Light Trapping Effect for Sensitive Infrared Photodetector and Image Sensing Application. *Adv. Funct. Mater.* **2019**, No. 1900849.
(36) Zhao, Y. D.; Qiao, J. S.; Yu, P.; Hu, Z. X.; Lin, Z. Y.; Lau, S. P.; Liu, Z.; Ji, W.; Chai, Y. Extraordinarily Strong Interlayer Interaction in 2D Layered PtS_2. *Adv. Mater.* **2016**, *28*, 2399−2407.
(37) Xie, C.; Nie, B.; Zeng, L. H.; Liang, F. X.; Wang, M. Z.; Luo, L. B.; Feng, M.; Yu, Y. Q.; Wu, C. Y.; Wu, Y. C.; Yu, S. H. Core-Shell Heterojunction of Silicon Nanowire Arrays and Carbon Quantum Dots for Photovoltaic Devices and Self-Driven Photodetectors. *ACS Nano* **2014**, *8*, 4015−4022.
(38) Lv, P.; Zhang, X. J.; Zhang, X. W.; Deng, W.; Jie, J. S. High-Sensitivity and Fast-Response Graphene/Crystalline Silicon Schottky Junction-based Near-IR Photodetectors. *IEEE Electron Device Lett.* **2013**, *34*, 1337−1339.
(39) Nie, B.; Hu, J. G.; Luo, L. B.; Xie, C.; Zeng, L. H.; Lv, P.; Li, F. Z.; Jie, J. S.; Feng, M.; Wu, C. Y.; Yu, Y. Q.; Yu, S. H. Monolayer Graphene Film on ZnO Nanorod Array for High-Performance Schottky Junction Ultraviolet Photodetectors. *Small* **2013**, *9*, 2872−2879.
(40) Liu, J. M. *Photonic Devices*; Cambridge University Press: Cambridge, 2005.
(41) Luo, L. B.; Chen, J. J.; Wang, M. Z.; Hu, H.; Wu, C. Y.; Li, Q.; Wang, L.; Huang, J. A.; Liang, F. X. Near-Infrared Light Photovoltaic Detector Based on GaAs Nanocone Array/Monolayer Graphene Schottky Junction. *Adv. Funct. Mater.* **2014**, *24*, 2794−2800.
(42) Xu, H.; Wu, J. X.; Feng, Q. L.; Mao, N. N.; Wang, C. M.; Zhang, J. High Responsivity and Gate Tunable Graphene-MoS_2 Hybrid Phototransistor. *Small* **2014**, *10*, 2300−2306.

https://dx.doi.org/10.1021/acsami.0c14996
ACS Appl. Mater. Interfaces XXXX, XXX, XXX−XXX

(43) Buscema, M.; Island, J. O.; Groenendijk, D. J.; Blanter, S. I.; Steele, G. A.; van der Zant, H. S. J.; Castellanos-Gomez, A. Photocurrent Generation with Two-Dimensional van der Waals Semiconductors. *Chem. Soc. Rev.* **2015**, *44*, 3691−3718.
(44) Xie, C.; Zeng, L. H.; Zhang, Z. X.; Tsang, Y. H.; Luo, L. B.; Lee, J. H. High-performance Broadband Heterojunction Photodetectors based on Multilayered $PtSe_2$ Directly Grown on a Si Substrate. *Nanoscale* **2018**, *10*, 15285−15293.
(45) Xiang, D.; Han, C.; Hu, Z. H.; Lei, B.; Liu, Y. Y.; Wang, L.; Hu, W. P.; Chen, W. Surface Transfer Doping-Induced, High-Performance Graphene/Silicon Schottky Junction-Based, Self-Powered Photodetector. *Small* **2015**, *11*, 4829−4836.
(46) Wang, L.; Jie, J. S.; Shao, Z. B.; Zhang, Q.; Zhang, X. H.; Wang, Y. M.; Sun, Z.; Lee, S. T. MoS_2/Si Heterojunction with Vertically Standing Layered Structure for Ultrafast, High-Detectivity, Self-Driven Visible-Near Infrared Photodetectors. *Adv. Funct. Mater.* **2015**, *25*, 2910−2919.
(47) Zeng, L. H.; Xie, C.; Tao, L. L.; Long, H.; Tang, C. Y.; Tsang, Y. H.; Jie, J. S. Bilayer Graphene Based Surface Passivation Enhanced Nano Structured Self-Powered Near-Infrared Photo-Detector. *Opt. Express* **2015**, *23*, 4839−4846.
(48) Yao, J. D.; Shao, J. M.; Wang, Y. X.; Zhao, Z. R.; Yang, G. W. Ultra-Broadband and High Response of the Bi_2Te_3−Si Heterojunction and Its Application as a Photodetector at Room Temperature in Harsh Working Environments. *Nanoscale* **2015**, *7*, 12535−12541.
(49) An, X.; Liu, F.; Jung, Y. J.; Kar, S. Tunable Graphene-Silicon Heterojunctions for Ultrasensitive Photodetection. *Nano Lett.* **2013**, *13*, 909−916.
(50) Mao, J.; Yu, Y. Q.; Wang, L.; Zhang, X. J.; Wang, Y. M.; Shao, Z. B.; Jie, J. S. Ultrafast, Broadband Photodetector Based on $MoSe_2$/Silicon Heterojunction with Vertically Standing Layered Structure Using Graphene as Transparent Electrode. *Adv. Sci.* **2016**, *3*, No. 1600018.
(51) Kresse, G.; Furthmüller, J. Efficient Iterative Schemes for Ab Initio Total-Energy Calculations Using a Plane-Wave Basis Set. *Phys. Rev. B* **1996**, *54*, 11169−11186.
(52) Tian, T.; Scullion, D.; Hughes, D.; Li, L. H.; Shih, C.-J.; Coleman, J.; Chhowalla, M.; Santos, E. J. G. Electronic Polarizability as the Fundamental Variable in the Dielectric Properties of Two-Dimensional Materials. *Nano Lett.* **2020**, *20*, 841−851.
(53) Perdew, J. P.; Burke, K.; Ernzerhof, M. Generalized Gradient Approximation Made Simple. *Phys. Rev. Lett.* **1996**, *77*, 3865−3868.
(54) Grimme, S.; Antony, J.; Ehrlich, S.; Krieg, S. A Consistent and Accurate Ab Initio Parametrization of Density Functional Dispersion Correction (DFT-D) for the 94 Elements H-Pu. *J. Chem. Phys.* **2010**, *132*, No. 154104.

https://dx.doi.org/10.1021/acsami.0c14996
ACS Appl. Mater. Interfaces XXXX, XXX, XXX−XXX